Photochemical age of air pollutants and oxidation products in transboundary air observed on Fukue Island, Nagasaki, Japan

Satoshi Irei,[1†] Akinori Takami,[1] Yasuhiro Sadanaga,[2] Susumu Nozoe,[1‡] Seiichiro Yonemura,[3] Hiroshi Bandow,[2] and Yoko Yokouchi[1]

[1]National Institute for Environmental Studies, 16-2 Onogawa, Tsukuba, Ibaraki 305-8506, Japan

[2]Department of Applied Chemistry, Graduate School of Engineering, Osaka Prefecture University, 1-1 Gakuencho, Naka-ku, Sakai, Osaka 599-8531, Japan

[3]National Institute for Agro-Environmental Sciences, 3-1-3 Kannondai, Tsukuba, Irabaki 305-8604, Japan.

[†] Present address: Department of Biology, Chemistry, and Marine Science, University of the Ryukyus, 1 Senbaru, Nishihara, Okinawa 903-0213, Japan.

[‡]Present address: National Museum of Emerging Science and Innovation, Aomi 2-3-6, Koto, Tokyo 135-0064, Japan.

Abstract

To better understand the secondary air pollution in transboundary air over westernmost Japan, ground-based field measurements of the chemical composition of fine particulate matter (≤1

μm), mixing ratios of trace gases species (CO, O_3, NO_x, NO_y, *i*-pentane, toluene, and ethyne), and meteorological elements were conducted with a suite of instrumentation. The CO mixing ratio dependence on wind direction showed that there was no significant influence from primary emission sources near the monitoring site, indicating long- and/or mid-range transport of the measured chemical species. Despite the considerably different atmospheric lifetimes of NO_y and CO, these mixing ratios were correlated (r^2 = 0.67). The photochemical age of the pollutants, *t*[OH] (the reaction time × the mean concentration of OH radical during the atmospheric transport), was calculated from both the NO_x/NO_y concentration ratio (NO_x/NO_y clock) and the toluene/ethyne concentration ratio (hydrocarbon clock). It was found that the toluene/ethyne concentration ratio was significantly influenced by dilution with background air containing 0.16 ppbv of ethyne, causing significant bias in the estimation of *t*[OH]. In contrast, the influence of the reaction of NO_x with O_3, a potentially biasing reaction channel on $[NO_x]/[NO_y]$, was small. The *t*[OH] values obtained with the NO_x/NO_y clock ranged from 2.9 $\times 10^5$ to 1.3×10^8 h molecule cm^{-3} and were compared with the fractional contribution of the *m*/*z* 44 signal to the total signal in the organic aerosol mass spectra (f_{44}, a quantitative oxidation indicator of carboxylic acids) and O_3 mixing ratio. The comparison of *t*[OH] with f_{44} showed evidence for a systematic increase of f_{44} as *t*[OH] increased, an indication of SOA formation. To a first approximation, the f_{44} increase rate was $(1.05 \pm 0.03) \times 10^{-9} \times [OH]\ h^{-1}$, which is comparable to the background-corrected increase rate observed during the New England Air

Quality Study in summer 2002. The similarity may imply the production of similar SOA component, possibly humic-like substances. Meanwhile, the comparison of *t*[OH] with O_3 mixing ratio showed that there was a strong proportional relationship between O_3 mixing ratio and *t*[OH]. A first approximation gave the increasing rate and background mixing ratio of ozone as $(3.48 \pm 0.06) \times 10^{-7} \times [OH]$ ppbv h^{-1} and 30.7 ppbv, respectively. The information given here can be used for prediction of secondary pollution magnitude in the outflow from the Chinese continent.

Key words:SOA; ozone; photooxidation of air pollutants; long-range transport; transboundary air pollution; East Asia

1. Introduction

During the last decade, the dramatic growth of the Chinese economy has increased emission of air pollutants such as volatile organic compounds, particulate matter (PM), and nitrogen oxides (NO_x), which is the sum of nitrogen monoxide (NO) and nitrogen dioxide (NO_2). In northeast Asia, air masses generally move from west to east, and therefore pollutants emitted on continental China are frequently carried to Japan. The influence of air pollution is becoming severe in rural areas of westernmost Japan, such as Fukue Island. Atmospheric oxidation of primary pollutants produces secondary pollutants, such as ozone (O_3), secondary particulate

58 organic matter (also known as secondary organic aerosol or SOA), which is formed by
59 oxidation of volatile organic precursors. A better understanding of these secondary pollutants
60 is important not only for purely scientific reasons but because such pollutants are a matter of
61 great public concern. SOA is one of the least understood subjects in atmospheric chemistry
62 (Ebben et al., 2014), despite the fact that it has been studied extensively owing to its potential
63 adverse effects on human health and its role in cloud condensation. Although state-of-the-art
64 techniques, such as aerosol mass spectrometry, have substantially improved our understanding
65 of SOA (Zhang et al., 2005; Jimenez et al., 2009), many questions about SOA still remain, such
66 as its constituents, production mechanisms, and fates.

67 To understand SOA, we must evaluate the progress of the chemical reactions of its
68 constituents. The progress of photochemical reactions in the atmosphere has frequently been
69 evaluated in terms of a "photochemical age," designated *t*[OH], which can be derived from
70 non-methane hydrocarbon (NMHC) ratios (Roberts et al., 1984; Rudolph and Johnen, 1990)
71 and from NO_x ratio to total odd nitrogen (NO_y) (Parrish et al., 1992). Recent field studies
72 combining aerosol mass spectrometry measurements and determination of *t*[OH] have
73 provided new information about photochemically produced SOA (de Gouw et al., 2005;
74 Takegawa et al., 2006; Kleinman et al., 2007; Liggio et al., 2010). Our previous field studies
75 conducted on Fukue Island in Japan demonstrated a systematic trend for the fractions of
76 carboxylate in the organic aerosol (f_{44}) with *t*[OH], evidence of SOA production (Irei et al.,

77 2014). However, the study period was short (only 10 days), and a longer observation period is
78 necessary to obtain more-convincing evidence of SOA production. Furthermore, inconsistent
79 results regarding the association between SOA production and *t*[OH] were observed at the same
80 location during a different time period (Irei et al., 2015). The study described in this paper is
81 an extension of our previous studies, and the objective was to deepen our understanding of the
82 association between oxidation products (SOA and O_3) and *t*[OH] in transboundary air.
83

84 **2. Experimental**

85 Field measurements were conducted from December 2010 to May 2011 at the Fukue
86 atmospheric monitoring station (32.8°N, 128.7°E), a rural site on the northwestern peninsula
87 of Fukue Island, Nagasaki Prefecture, Japan (Figure 1). As mentioned earlier, data collected
88 during a 10 day observation period in December 2010 have already been reported, and the
89 reported results are a part of data in this study. The monitoring station is ~1 km away from the
90 residential area of the peninsula and is ~60 m higher in altitude. The site is located in-between
91 small pastures. Possible sources of anthropogenic emissions of fine aerosol and trace gas
92 species include agricultural waste burning, home incinerators, automobiles occasionally
93 passing by the station, and tractors sometime mowing the pastures. For all the measurements
94 the ambient air was measured or sampled 1 ~ 3m above the rooftop of the station (3 ~ 5m height
95 from the ground). An independent sampling line was assembled for each chemical species

96 measurement. The ambient air was sampled at 1 L min^{-1} through 5 m × quarter-inch o.d. PTFE
97 tubing for the CO and O_3 measurements and at 0.5 L min^{-1} through the same type of tubing for
98 the NO_x and NO_y measurements, respectively. A molybdenum converter for the NO_y
99 measurements was set at the inlet of sampling line. For the particle and NMHC measurements,
100 the ambient air was suctioned at 3 L min^{-1} and 5 L min^{-1} at the first stage through the sampling
101 lines of ~4 m × half-inch o.d. and ~10 m × five-fifth-inch o.d. stainless steel tubing (GL Science,
102 Japan), respectively. The measurements were then made by sampling a part of the flowing air.
103 For the particle measurements only, a $PM_{2.5}$ cyclone separator (URG 2000-30ED, URG Corp.
104 Chapel Hill, NC, USA.) was attached to the inlet of the sampling line to cut off particles larger
105 than $PM_{2.5}$.

106 The 10 min average chemical composition of fine aerosol (~$PM_{1.0}$) was measured with
107 an Aerodyne quadrupole aerosol mass spectrometer (AMS, Aerodyne Research Inc., Billerica,
108 MA, USA). Details of the instrumentation and the method for determination of chemical
109 species concentrations are described elsewhere (Jayne et al., 2000; Allan et al., 2004). The
110 AMS was calibrated approximately once a month with 350 nm dried ammonium nitrate
111 particles for determination of ionization efficiencies. The temperature of the flash vaporizer
112 was set to 873 K during the field measurements and calibration measurements. A collection
113 efficiency of 0.74 was used for determination of chemical species concentrations; this value
114 was determined from comparison between sulfate concentrations measured by means of AMS

and non-sea-salt sulfate concentrations determined by means of total suspended particulate filter sample analysis during the field study in December 2010 (Irei et al., 2014). The detection limits (DLs) of the mass spectrometer for chloride, nitrate, ammonium, sulfate, organics, *m*/*z* 43 (an indicator for detection of hydrocarbon and aldehyde) , and *m*/*z* 44 (an indicator for detection of carboxylic acid) were determined by 3 × standard deviation (SD) of blank concentrations obtained by measuring filtered ambient air (HEPA Capsule, Pall Corp.) for 2 ~ 16 hours. The blank measurements were conducted every month during the study period. The average DLs of these species were 0.02, 0.04, 0.2, 0.4, 0.5, 0.02, and 0.06 μg m^{-3}, respectively.

Mixing ratios for NO_x and NO_y were measured in situ to retrieve the *t*[OH], an indicator of atmospheric oxidation. Measurement methods for NO_x and NO_y mixing ratios were developed with an LED converter and a molybdenum converter, respectively, together with commercially available NO_x analyzers (Model 42 i-TL, Thermo Scientific). These instruments are described in detail elsewhere (Sadanaga et al., 2010; Yuba et al., 2010). DLs for NO, NO_2, and NO_y were about 0.06 ppbv under 1 min averaging time. Mixing ratios of CO and O_3 were measured in situ with a CO analyzer (Model 48, Thermo Scientific) and an O_3 analyzer (Model 49i, Thermo Scientific), respectively. The DLs of these instruments were 3 and 5 ppbv under 1 min averaging time, respectively. The analog signal output for these trace gas species was recorded every second using a data logger (NR-1000, KEYENCE), and hourly average mixing ratios were used for data analysis. Selected NMHCs (ethyne, *i*-pentane, and toluene) were also

134 measured hourly with a gas chromatograph equipped with a flame ionization detector (6890N,
135 Agilent Technologies) and coupled with an automated cryo preconcentration sampler
136 (Yokouchi, 2008). Ethyne, *i*-pentane, and toluene were chosen because those can be used as
137 markers for vehicular emissions (Tang et al., 2009; Wang et al., 2015). The choice of toluene
138 was also owing to one of the possible precursors of atmospheric SOA (Grosjean and Seinfeld,
139 1989; Seinfeld and Pandis, 1999). The volatile organic compounds in 600 mL of ambient air
140 were collected cryogenically from the main stream of the previously referred sampling line at
141 a flow rate of 40 mL min^{-1} (*i.e.*, a 15 min sampling period for a single measurement). Target
142 compounds were identified and quantified on the basis of comparison with retention times and
143 peak area counts for standards; specifically, a standard gas containing 1 ppb of each target
144 compound was analyzed once a day. The DLs for ethyne, *i*-pentane, and toluene were 2,5, 1.5,
145 and 1.5 pptv, respectively.

146 Additionally, ambient temperature, relative humidity (RH), precipitation, and wind
147 speed and direction were measured with a weather transmitter (WXT 520, VAISALA, Helsinki,
148 Finland).

149

150 **3. Results and Discussion**

151 **3.1. Meteorological observations**

152 Measured ambient temperature ranged from 274.6 to 301.2 K, the mean ± standard deviation

153 or SD = 286.6 ± 5.4 K (Figure S-1). Ambient temperature showed clear seasonal variation, and
154 a polynomial best fit curve ± 5 K covered ~90% of the data points and reproduced the observed
155 trend.

156 Precipitation events were observed occasionally (Figure S-1), but their frequency and
157 strength did not seem to significantly affect our overall interpretation of the entire data set.
158 Therefore, in the analyses described hereafter, we included the data collected during the
159 precipitation events, unless otherwise noted. RH varied between 25% and 100% and seemed
160 to be relatively constant from December to February and to vary more widely from March to
161 May (Figure S-1).

162 A polar plot of hourly average wind speed shows that it ranged from 0.2 to 10 m s^{-1}
163 (Figure S-2). The mean ± SD of wind speeds during the observation period was 3 ± 1 m s^{-1},
164 and the 90th, 25th, and 10th percentile cut-off values were 4, 2, and 1 m s^{-1}, respectively. This
165 information suggests that medium-strength winds (i.e., wind speeds of 2–4 m s^{-1}) blew most of
166 the time during the study period. Because wind directions measured at wind speeds of <1 m s^{-1}
167 are often treated as invalid, the fact that the 10th percentile cut-off for our data was 1 m s^{-1}
168 indicates that 90% of our wind direction data were valid. The most prevalent wind directions
169 were between northwesterly and northeasterly (35%) and between northeasterly and
170 southeasterly (26%). The prevalence of wind from the residential area of the peninsula (from
171 the direction between southeasterly and southwesterly) was about 17%.

172

173 **3.2. Chemical species concentrations**

174 The results of statistical analysis of the concentrations of chemical species in fine PM are
175 summarized in Table 1, along with the results for gas-phase species. Because sea-salt PM tends
176 to be coarse, the very low concentrations of chloride measured by means of AMS indicate that
177 most of the chloride originating from sea salt was eliminated at the AMS inlet, which selects
178 for fine PM. The mean concentrations (± SDs) of the chemical species in fine PM were similar
179 to those observed in 2003 at the same location (Takami et al., 2005) and at Cape Hedo, Okinawa
180 (Takami et al., 2007). Sulfate was the predominant chemical species in fine PM throughout the
181 observation period, accounting for 46% on average, and was followed by organics (29%),
182 ammonium (16%), and nitrate (8.0%). The concentrations of nitrate, the detection of which is
183 often an indication of the proximity of its emission source, were high in this study even though
184 the monitoring station was located in a rural area. In many cases, the amount of nitrate in fine
185 PM decreases or shifts to larger PM during long-range transport (Takiguchi et al., 2008, and
186 references therein). Because there are no large emission sources of primary nitrate around the
187 monitoring station, the high nitrate concentrations probably indicate mid-range transport of
188 pollutants from locations off the island. Temporal variation of the concentrations of organics
189 in fine PM measured by means of AMS showed no seasonal trend, but some high-concentration
190 episodes were observed (Figure S-3). It was also found that the concentrations of organic

aerosols in the study period from 6 to 16 December, which was previously reported (Irei et al., 2014), were relatively low. In the time-series plot, the f_{44}, the fraction of *m*/*z* 44 in the organic mass spectrum or the fraction of carboxylate in organic aerosol, seemed to rise from ~0.12 to ~0.15 around the end of March. This increase may have been due to greater production of oxygenated organic compounds in spring than in winter because of the increasing sunlight irradiance in the spring, which was indicated by the times-series plot of ambient temperature (Figure S-1).

Most of the O_3 mixing ratios were <55 ppbv, and the mean of 45 ppbv was consistent with the annual mean of ~50 ppbv observed at the same location in 2011 (Kanaya et al., 2016); this annual mean of ~50 ppbv was the lowest annual mean O_3 mixing ratio observed over the course of 6 years (2009 − 2014) at this location by Kanaya et al. A times-series plot of hourly average O_3 mixing ratios showed that although there were some episodes of high mixing ratios, the mixing ratios seemed to vary between ~25 and ~50 ppbv from December to February and then were prone to gradually increase from the beginning of March to May (Figure S-4a). Similar seasonal trends have been observed at the same location (Kanaya et al., 2016) and at other remote sites in East Asia (Pochanart et al., 2002; Suthawaree et al., 2008; Kanaya et al., 2016, references therein). This trend was similar to the f_{44} trend described above and therefore can also be explained in terms of an increase in sunlight irradiance of polluted air masses transported from the Asian continent. Meanwhile, according to the observations at the other

remote sites referred above, the O_3 mixing ratios tend to drop starting in May and continuing into the summer because the origin of air masses changes from the continent directly to the Pacific Ocean; the oceanic air masses generally contain much lower quantities of O_3 and its precursors. The drop in the O_3 mixing ratios observed between May 9 and May 12 was compatible with the influence of the oceanic air masses demonstrated by the back trajectories of air masses (Figure S-5) modeled by HYSPLIT (Draxler and Rolph, 2013).

The NO_x mixing ratios ranged from lower than the DL (LDL) to 12.70 ppbv (mean ± SD = 1.39 ± 1.16 ppbv), and the NO_y mixing ratios ranged from 0.13 to 25.41 ppbv (mean ± SD = 4.86 ± 3.49 ppbv). The upper quartile cut-offs for these mixing ratios were 1.70 and 6.03 ppbv, respectively. NO was found to be the very minor component of NO_x. The median and lower and upper quartile cut-off values of NO were LDL, LDL, and 0.06 ppbv, respectively. Compared to the mixing ratios observed in other field studies (Pandey Deolal et al., 2012, and references therein), most of these mixing ratios fell between those observed at European rural and background sites. No time-dependent trend was observed for the NO_x or NO_y mixing ratio (Figure S-4b,c). Episodes of high mixing ratios were observed irregularly.

The CO mixing ratios ranged from 57 to 1136 ppbv, and the median, upper, and lower quartile cut-off values were 204, 272, and 160 ppbv, respectively; no seasonal trend was observed (Figure S-4d). Except for some episodes of high mixing ratios, the observed mixing ratios below the upper quartile cut-off seem to be comparable in magnitude to those observed

229 from 2002 to 2005 at various rural and remote locations in the region of the East China Sea
230 (Suthawaree et al., 2008; Tanimoto et al., 2008), indicating that the mixing ratios we observed
231 reflected the background mixing ratios in this region. A polar plot of the wind-sector
232 dependence of the CO mixing ratio showed almost no sharp increases attributable to local
233 anthropogenic emissions (Figure S-6). The episodes of high mixing ratios that occurred at
234 irregular intervals were attributed to mid-range transport of anthropogenic emissions.

235 To determine whether these episodes were due to combustion-related pollution
236 transported from the Asian continent, we chose seven time periods with high CO mixing ratios
237 that lasted for more than 24 h, and we checked the back trajectories of the air masses modeled
238 by HYSPLIT. These episodes are listed in Table S-1, together with confirmation of
239 concentration rises of other chemical species during the high-CO episodes. Back trajectories
240 for each episode showed that the air masses were transported from the region of east-coast of
241 China or of west coast of Korea during these episodes. The trajectories also showed that the
242 episodes ended with the arrival of air masses from the Pacific Ocean or Mongolia with greater
243 wind speed (Figures S-7 to S-13). Thus, these results roughly support the proposition that at
244 least these seven high-concentration episodes were derived from the Asian continent.

245 Most of the observed mixing ratios for *i*-pentane, toluene, and ethyne (Table 1) were
246 slightly higher than the ratios observed at Cape Hedo, Okinawa, in 2000 (Kato et al., 2004).
247 This result is consistent with the fact that pollutants transported from the Asian continent to

248 Fukue are often fresher than those transported to Cape Hedo (Takami et al., 2007). Times-series
249 plots of the mixing ratios for these NMHCs showed no seasonal trends (Figure S-4e–g). The
250 observed sharp rises in mixing ratios of *i*-pentane, toluene, and ethyne—which lasted no more
251 than a few hours, indicating the influence of anthropogenic emissions near the site—accounted
252 for only a small portion of the observed data.
253
254 **3.3. Correlations between the concentrations of various chemical species**
255 Investigation of the correlations between the concentrations of various chemical species
256 showed that CO concentration was correlated with the concentrations of NO_y (r^2 = 0.674),
257 ethyne (r^2 = 0.724), and organic aerosols (r^2 = 0.562) (Table 2). Ethyne is a combustion marker
258 and often originate from vehicular emission, which is one of the major sources of NO_x as well.
259 The atmospheric lifetimes of CO and ethyne are usually determined by the reactions with OH
260 radicals (the most powerful oxidant in the air). Under an average OH concentration of 5×10^5
261 molecules cm^{-3}, which is the calculated diurnally averaged OH concentration during the
262 PEACE-A aircraft campaign over Japan in January 2002 (Takegawa et al., 2004), their lifetimes
263 are approximately 100 and 35 days, respectively. Meanwhile, they found experimentally that
264 the lifetime of NO_y during the campaign was 1.3 ~ 2.6 days, which was mainly due to the wet
265 and/or dry depositions of HNO_3. That is, ~60% of NO_y sinks within 2.6 days. Because the
266 processes are physical we expect that the order of NO_y lifetime in our study is similar. The

267 slope of the linear regression drawn for the NO_y mixing ratio as a function of CO mixing ratio
268 was approximately 0.03, which is in the similar order to the value of ~0.038 observed by
269 Takegawa et al. in the 2~3 day aged plume originated from Japan. The slope also coincided
270 with the calculated NOy/CO ratio of 0.03 in an air mass transported a long distance from its
271 origin to Korea using a recent emission inventory (Kim et al., 2012). In contrast, Kurokawa et
272 al. (2013) reported that emission ratios of NO_x to CO from coal combustion used in industry in
273 China, which is suspected to be one of the major sources of these pollutants observed in our
274 study, were 0.06 ~ 0.07. With consideration of the NO_y lifetime by the depositions and the
275 transport time of roughly 1 ~ 3 day implied by the back trajectories previously referred, the
276 discrepancy between the NO_y/CO observed at Fukue and the NO_x/CO at emission seems to be
277 reasonably explained by the depositional sink during the transport. The higher coefficient of
278 determination between CO and ethyne than that between CO and NO_y also supports the
279 association of their correlation with their lifetimes. Nevertheless of such significant
280 depositional loss of NO_y, the positive correlation with the r^2 of 0.674 between CO and NO_y
281 implies that the wet deposition, which is highly variable and influential, did not significantly
282 contribute to the NO_y sink, in turn, the major sinking process of NO_y was the dry deposition
283 depending on the gravitational residence time.

284 Particulate ammonium was correlated with particulate acidic components, such as
285 sulfate, nitrate, organics, and m/z 44 of organics. The highest correlation with *m/z* 44 (r^2 =

286 0.755) suggests that the organics were primarily composed of carboxylic acids. The observed
287 correlations imply that sufficient amount of ammonium was available in the gas-phase to
288 neutralize all these acidic components. Although it is not shown, slopes of linear regressions
289 between ammonium (*x*-axis) and sulfate, nitrate, or organics (*y*-axis) was 1.7, 0.74, and 1.0,
290 respectively. With respect to molar ratio to ammonium, sulfate and nitrate accounted for 32%
291 and 20%, respectively. Given that all three acidic species are neutralized with ammonium,
292 organics, molar mass of which is unknown, accounts for 16%. This number in turn gives the
293 average molecular weight of organics as 113 g mol^{-1} for monocarboxylate.

294 The overall correlation between *m*/*z* 43 and *m*/*z* 44 in the organic mass spectra obtained
295 by AMS was 0.640, but a plot of *m*/*z* 43 versus *m*/*z* 44 showed two distinct trends: a trend with
296 an *m*/*z* 44 to *m*/*z* 43 ratio of ~1 and another with a ratio of ~2.5 (Figure S-14). This result
297 suggests that two types of organic species gave fragment ions that contributed to the *m*/*z* 44 to
298 *m*/*z* 43 ratio. These species will be discussed in detail in Sect. 3.4.

299

300 **3.4. Oxidation state of organic aerosols**

301 As we did in previous reports for the field studies in December 2010 (Irei et al., 2014) and in
302 March 2012 (Irei et al., 2015), here we briefly discuss the results of evaluation of the oxidation
303 state of the organic aerosols observed during the half-year period of this study. First, we applied
304 positive matrix factorization (PMF) analysis to the organic aerosol mass spectra to deconvolute

the types of organic aerosols (Zhang et al., 2005; Ulbrich et al., 2009), and then we determined the oxidation state of each type of organic aerosol by plotting the fractions of *m*/*z* 43 (f_{43}) and *m*/*z* 44 (f_{44}) in the organic mass spectra, according to the method described by Ng et al. (2010). Furthermore, we determined the mass to carbon ratios (OM/OC ratios) of the types of organic aerosol using the method described by Zhang et al. (2005) to characterize the species of the organic aerosols.

With respect to the mass spectral pattern, PMF analysis gave the most feasible solution with two types of organic aerosols: hydrocarbon-like organic aerosol (HOA) and low-volatility oxygenated organic aerosol (LV-OOA) (Figure 2). The mass spectral patterns of these two types of aerosols agreed well with those of HOA and LV-OOA found in the December study (r^2 of 0.98 and 0.98, respectively). The patterns also agreed reasonably with the reference mass spectra for HOA and LV-OOA in the AMS spectral database (r^2 of 0.94 and 0.53, respectively) made available by Ulbrich et al. (http://cires.colorado.edu/jimenez-group/AMSsd/). The time-series variations of the HOA and LV-OOA mass concentrations showed similar patterns (Figure 3), an implication that the primary OA and the precursor(s) of LV-OOA are from the same source in large scale. On average, HOA and LV-OOA accounted for 38% and 59% of the organic aerosols throughout the study period, respectively. These values are in the same magnitude to the fractions previously reported during the study in December 2010 (32% and 67% for HOA and LV-OOA, respectively). In a plot of f_{43} versus f_{44}, the data point of f_{43} and

f_{44} for LV-OOA in this study was located at the top of the triangle, indicating a high oxidation state (Figure 4). The OM/OC ratio of HOA and LV-OOA were 2.8 and 5.0 μg μgC^{-1}, respectively. The OM/OC ratio of HOA was twice as high as the ratio of HOA found in the December study. This may be an implication of oxidation of HOA at some extent. The OM/OC ratio of LV-OOA was 1.4 and 1.2 times as high as the ratios of LV-OOA found in our field studies in December 2010 and March 2012, respectively. To the best of our knowledge, substances showing such a high OM/OC ratio are only humic-like substances.

3.5. Chemical clocks

We used a NO_x/NO_y concentration ratio and a NMHC concentration ratio to explore the extent of photochemical reaction (*i.e.*, the reaction with OH radical). In this type of chemical clock analysis, the concentration of a reactive chemical and that of a less reactive chemical are used in the numerator and the denominator, respectively, of the ratio. As a reaction proceeds, the numerator decreases while the denominator remains constant; therefore, a change in the ratio indicates the extent of reaction. In application of chemical clocks to the atmospheric transport of pollutants, users should be aware of that the extent of reaction may not always be well defined because emission sources are spatially distributed over the trajectory of an air parcel in many cases. This type of analysis is ideally suited to situations in which inputs into an air parcel from additional emission sources during transport are negligible. Our field study for

343 transboundary air pollution transported over the East China Sea can be the ideal case.

344

345 **3.5.1. NO_x/NO_y clock**

346 To see if such an assumption is valid, the NO_x/NO_y and hydrocarbon clocks were evaluated.
347 Given that the conversion of NO_2 (the major component of NO_x) to HNO_3 (one of the
348 components of NO_y)

349 $$NO_2 + OH \xrightarrow{M} HNO_3 \qquad (R1)$$

350 is the major sink for NO_x and that the concentration of OH radicals, [OH], can be assumed to
351 be constant, the photochemical age, t[OH], of NO_x can be determined according to the
352 following pseudo-first order rate law:

353 $$t[\mathrm{OH}] = -\frac{1}{k_{NO_2}} \ln \frac{[NO_x]}{[NO_y]} \qquad (1)$$

354 where $[NO_x]$, $[NO_y]$, and k_{NO2} are the concentrations of NO_x and NO_y (molecules cm^{-3}) at
355 reaction time t and the temperature-dependent effective second-order rate constant for the
356 reaction of NO_x with OH radicals, respectively. k_{NO2} includes the concentration of a third body,
357 [M], which depends on pressure and temperature. To calculate k_{NO2} at ambient temperature and
358 a pressure of 1 atm, we therefore calculated the third-order rate constant and [M] according to
359 the method described by Finlayson-Pitts and Pitts (2000) with the polynomial best fit for
360 measured ambient temperature mentioned in Sect. 3.1. The calculated k_{NO2} values at 1 atm
361 ranged from 9.3×10^{-12} to 1.1×10^{-11} cm^3 $molecule^{-1}$ s^{-1}, and both the mean and the median

were 1.0×10^{-11} cm^3 $molecule^{-1}$ s^{-1}. In turn, the determined t[OH] using the k_{NO2} values and the $[NO_x]/[NO_y]$ ratios ranged from 2.9×10^5 to 1.3×10^8 (mean ± SD = $(3.4 \pm 1.6) \times 10^7$ h molecules cm^{-3}). We found that the use of a fixed k_{NO2} value (i.e., the mean value of 1.0×10^{-11} cm^3 $molecule^{-1}$ s^{-1}) resulted in biases between –10% and +7% in the estimation of t[OH]. We also found that a temperature variation of ± 5 K resulted in only a ± 5% variation in t[OH]. However, this analysis for the biases does not take into account temperature and pressure variations during the transport of the air parcels.

The reaction of NO_2 with O_3, which may result in significant overestimation in the NO_x/NO_y clock, was also evaluated. The reaction of NO_2 with O_3 forms NO_3 radicals:

$$NO_2 + O_3 \longrightarrow NO_3 + O_2 \qquad \text{(R2)}$$

This reaction channel is important at night, but negligible during the day when NO_3 radicals are quickly photolyzed back to NO_x. NO_3 radicals react with NO_2 to form stable N_2O_5, which is in thermal equilibrium with NO_2 and NO_3 and therefore acts as a reservoir of NO_x:

$$NO_2 + NO_3 \leftrightarrow N_2O_5 \qquad \text{(R3)}$$

N_2O_5 reacts slowly with water vapor to form HNO_3, and this process terminates the chain reaction:

$$N_2O_5 + 2H_2O \longrightarrow 2HNO_3 \qquad \text{(R4)}$$

The reaction of N_2O_5 with water vapor is a dominant reaction channel when the RH is above 50% (Finlayson-Pitts and Pitts, 2000, and references therein), which can be the case in our

study (Figure S-1). Although the contribution of the reaction of NO_2 with O_3 may result in a significant overestimation of *t*[OH], one should remind that the R4 channel is negligible as there is enough ammonia to neutralize sulfate (Brown et al., 2006), which is our case.

We evaluated the significance of this reaction channel by comparing the lifetime of NO_x with respect to reaction with OH radicals (R1 channel), τ_{OH}, and with respect to reaction with O_3 (R2 channel), τ_{O3}, at constant OH radical and O_3 concentrations. For this evaluation, we used 1.0×10^{-11} and 3.2×10^{-17} cm^3 $molecule^{-1}$ s^{-1} at 298 K and 1 atm as the second-order rate constants for the two reactions, respectively, and 5×10^5 and 1.3×10^{12} molecules cm^{-3} (0.021 pptv and 52 ppbv) as the OH and O_3 concentrations, respectively. The OH concentration was chosen because 5×10^5 molecules cm^{-3} was the reasonable value in our previous study (Irei et al., 2014), and the O_3 concentration was chosen because the concentration was the upper quartile cut-off value of the observed O_3 in this study. The values of τ_{OH} and τ_{O3} were calculated to be 54 and 6.8 h, respectively. That is, the R2 was approximately 4 times as fast as the R1 under these conditions. If the reaction of NO_2 with O_3 at night was the predominant mode of conversion of NO_x to NO_y, a positive correlation between the O_3 mixing ratio and the extent of NO_x turnover—that is, between the O_3 mixing ratio and $\ln([NO_x]/[NO_y])$—should be observed in our night time data. However, a plot of the hourly O_3 mixing ratios versus hourly $\ln([NO_x]/[NO_y])$ showed no positive correlation, but a clear inverse correlation ($r^2 = 0.489$), indicating that the turnover of NO_x to NO_y increased as the O_3 mixing ratio increased (Figure

400 5). Similar observations have been reported elsewhere (Olszyna et al., 1994; Roussel et al.,
401 1996). Given that during the day, O_3 forms only photochemically, this inverse correlation
402 suggests that NO_x conversion was due to daytime photochemistry. A conclusion with this
403 possibility was drawn from an analysis of O_3 production efficiency (Yokouchi et al., 2011).

404 The photochemical reaction of aldehydes is also a sink for NO_2, resulting in the
405 formation of thermally stable peroxyacyl nitrates:

406 $$RCHO + OH \longrightarrow RCO + H_2O \qquad (R5)$$

407 $$RCO + O_2 \longrightarrow RC(O)OO \qquad (R6)$$

408 $$RC(O)OO + NO_2 \longrightarrow RC(O)OONO_2 \qquad (R7)$$

409 Unfortunately, we cannot evaluate the significance of this channel with our current dataset,
410 because no data for aldehyde and peroxyacyl radical concentrations are available. Because this
411 loss channel also occurs in sunlight, the possibility that peroxyacyl nitrate formation
412 significantly affects *t*[OH] cannot be excluded. The absolute value of *t*[OH] derived from the
413 $[NO_x]/[NO_y]$ ratio remains uncertain, but as demonstrated by the high correlation between this
414 ratio and the O_3 mixing ratio, the use of the NO_x/NO_y clock nevertheless provides valuable
415 information about the relative extent of photooxidation. When we plotted the time-series
416 variation of *t*[OH] estimated from the $[NO_x]/[NO_y]$ ratio (Figure 6), we observed variation
417 similar to that observed for the hourly average O_3 mixing ratio (Figure S-4a), implying a strong
418 association between the *t*[OH] and the sunlight irradiance.

3.5.2. Hydrocarbon clock

When NMHC A and B react with OH radicals at different rate

$$A + OH \longrightarrow Product + H_2O \quad \text{(R8)}$$

$$B + OH \longrightarrow Product + H_2O \quad \text{(R9)}$$

t[OH] can also be estimated from the ratio of the two NMHCs (Robert et al., 1984; Rudolph and Johnen, 1990; Parrish et al., 1992):

$$t[OH] = \frac{1}{(k_A - k_B)} \ln\left(\frac{[A_0]}{[B_0]} \cdot \frac{[B]}{[A]}\right) \quad (2)$$

where $[A_0]$ and $[B_0]$ are the initial concentrations (molecules cm^{-3}) of NMHCs A and B, which have short and long lifetimes (relative to each other); [A] and [B] are the concentrations (molecules cm^{-3}) at time *t*; and k_A, and k_B are the temperature-dependent rate constants for reactions of A and B with OH radicals (molecules^{-1} cm^3 s^{-1}). If NMHCs A and B are emitted from the same source at the same time, the change in the concentration ratio theoretically indicates the extent of chemical reaction. However, dilution with an aged air mass containing depleted NMHCs can also change the NMHC ratio, thus biasing the *t*[OH] estimation (McKeen and Liu, 1993). This bias can be visualized by plotting two different NMHC ratios with the same denominator, and we used the [*i*-pentane]/[ethyne] and [toluene]/[ethyne] ratios for this evaluation. The calculations require the rate constants for the reactions of the NMHCs with OH radicals under the mean temperature observed, 283.7 K, the mixing ratios of the NMHCs in the

438 background air, and their initial mixing ratios at emission. Using the Arrhenius equation with
439 the recommended parameters for *i*-pentane, toluene, and ethyne (NIST Chemistry WebBook,
440 http://webbook.nist.gov/chemistry/), respectively, the rate constants for the reaction of these
441 compounds with OH radicals at 283 K (*i.e.*, the mean temperature during the study period)
442 were calculated to be 3.44×10^{-12}, 5.88×10^{-12}, and 7.38×10^{-13} cm^3 $molecule^{-1}$ s^{-1}, respectively.
443 Note that the variation of the slope for the reaction loss owing to the variation of the
444 temperature-dependent rate constants between the maximum and minimum temperature (298.3
445 and 271.5 K) was found to be less than ± 2%. Thus, the variation of the reactive loss due to the
446 temperature change was not influential to our analysis. For the background mixing ratios, we
447 used mixing ratios observed at Cape Hedo, Okinawa (Kato et al., 2004), which were 0.05, 0.09,
448 and 0.39 ppbv, respectively. For the initial mixing ratios at emission, we used the reported
449 scores for loadings extracted by means of PMF analysis for the NMHC sources in Beijing
450 (Wang et al., 2015). The PMF loadings used in the calculations were vehicular emissions 1 and
451 2, solvent use, and natural gas and gasoline leakage. In addition to these initial mixing ratios,
452 mixing ratios reported a rural site in northeast China (Lin'an, in the Yangtze River Delta, Tang
453 et al., 2009) were also tested.

454 The plot shows that, with respect to the initial NMHC ratio, depletion trends resulting
455 from use of the solvent-use profile and of the observations in Lin'an deviated substantially
456 from the observed overall trend (Figure 7). The majority of observed plots lies between the

457 trends for the dilution with the background air and the reaction loss calculated if the profiles
458 for the vehicular-emissions and natural-gas and gasoline leakage were used. That is, the
459 vehicular emissions and the natural gas and gasoline leakage may have been the predominant
460 emitters of these NMHCs, but source apportionment is difficult because of the uncertainty in
461 the emission profiles. On the basis of this comparison, we could identify only two possible
462 significant sources of these NMHCs during the measurement period. The layout of observed
463 data points in-between the dilution and reactive loss lines also suggests that depletion in their
464 mixing ratios was a combination of these processes. Comparison of calculated *t*[OH] by the
465 toluene/ethyne clock with those by the NO_x/NO_y clock exhibited a poor correlation (Figure S-
466 15), demonstrating the limitation of the toluene/ethyne clock for estimation of *t*[OH] under the
467 condition at Fukue. A quantitative understanding will require a more sophisticated analysis
468 based on mass balance with reliable source profiles.

469 With respect to the background mixing ratios observed at Cape Hedo, the plot also
470 shows that many of our observed data points were lower than the background NMHC ratios
471 represented by a brown circle in Figure 7. This result implies that the background NMHC ratios
472 from the observations at Cape Hedo are still too high to be used as background values of these
473 NMHC ratios for the study region. It is reasonable to assume that the background mixing ratios
474 for both toluene and *i*-pentane in the aged air masses were LDL (<3 pptv). This assumption
475 allows us to approximate the background mixing ratio of ethyne based on the smallest

476 [toluene]/[ethyne] and [*i*-pentane]/[ethyne] ratios observed. According to the plot, the use of –
477 3.5 for the ln[toluene]/[ethyne] and –4 for ln[*i*-pentane]/[ethyne], approximately the smallest
478 ratios observed, seems more reasonable. If we use the highest DL value (3 pptv) as the
479 background mixing ratio for toluene and *i*-pentane, the background ethyne mixing ratio is then
480 calculated to be ~0.16 ppbv, which is about 25% of the background value observed at Cape
481 Hedo by Kato et al. (2004). On the basis of the plot in Figure 7, we recommend the use of
482 0.003, 0.003, and 0.16 ppbv as the background mixing ratios for *i*-pentane, toluene, and ethyne,
483 respectively, in the region of the East China Sea.
484
485 **3.6. Dependence of f_{44} and O_3 on *t*[OH]**
486 A scatter plot of f_{44} as a function of *t*[OH] estimated by the NO_x/NO_y clock showed a
487 proportional increase of f_{44} with increasing *t*[OH] (estimated by means of the NO_x/NO_y clock)
488 up to a *t*[OH] value of 7×10^7 h molecules cm^{-3}, and then f_{44} started to level off slightly (Figure
489 8). That is, f_{44} works as an oxidation indicator below the *t*[OH] of 7×10^7 h molecules cm^{-3}.
490 The f_{44} oxidation indicator is known to be case dependent, even at this location and below this
491 upper limit (Irei et al., 2015). Considering the existence of HOA during the study period, a
492 series of findings here and in the previous reports supports our hypothesis that f_{44} varies with
493 *t*[OH] as LV-OOA, which has a constant and high value of f_{44}, mixes with the background-level
494 HOA, which has a significantly lower constant value of f_{44} than LV-OOA (Irei et al., 2014). To

a first approximation of the increasing trend, f_{44} is given by

$$f_{44} = (1.05 \pm 0.03) \times 10^{-9} t[\mathrm{OH}] + 0.103 \pm 0.001 \quad (3)$$

with an r^2 value of 0.369. The first approximation satisfactorily describes the increasing trend below a t[OH] value of 7×10^7 h molecules cm^{-3}. The intercept of the first approximation indicates the f_{44} value for organic aerosol at a photochemical age of zero, that is, f_{44} at emission. The slope, which was $(1.05 \pm 0.03) \times 10^{-9}$ h^{-1} $molecule^{-1}$ cm^3, indicates the rate of increase of f_{44} as [OH] is given. Kleinman et al. (2007) observed that during the New England Air Quality Study, the background-corrected f_{44} value increased from 0.08 to 0.13 as $-\ln([NO_x]/[NO_y])$ increased from 0.1 to 1.3, which corresponds to an increase of t[OH] from 3.2×10^6 to 42×10^6 h molecule cm^{-3}. These values give an increase rate of $1.3 \times 10^{-9} \times$[OH] h^{-1}, which is almost identical to the rate we calculated in this study. The overall proportionality of f_{44} with t[OH] suggests that, like the NO_x/NO_y clock, f_{44} worked as an oxidation indicator during this study period. This, however, is inconsistent with our another report, in which no proportional increase of f_{44} was observed during the study in different year at the same location (Irei et al., 2015). Interestingly, our hypothesis of binary mixture of organic aerosol is still consistent with these contradicting cases.

It has been proposed that the increasing trend of f_{44} can be explained by a binary mixture of variable amount of LV-OOA depending on extent of reaction processing x for the LV-OOA precursor and constant amount of HOA (Irei et al., 2014, Supporting Information):

$$f_{44} = \frac{{}^{HOA}f_{44} \cdot a \cdot (\frac{OM}{OC})_{HOA} + {}^{LVOOA}f_{44} \cdot \left[0.3x \cdot b \cdot (\frac{OM}{OC})_{LVOOA} \right]}{a \cdot (\frac{OM}{OC})_{HOA} + \left[0.3x \cdot b \cdot (\frac{OM}{OC})_{LVOOA} \right]} \quad (4)$$

In this equation ${}^{HOA}f_{44}$ and ${}^{LV\text{-}OOA}f_{44}$ are the fractions of m/z 44 signal for the HOA and LV-OOA factors from the PMF analysis previously discussed, respectively; $(OM/OC)_{HOA}$ and $(OM/OC)_{LV\text{-}OOA}$ are the organic mass concentration ratios to the organic carbon concentrations ($\mu g\ \mu gC^{-1}$) for the HOA and LV-OOA from the PMF analysis, respectively; and *a* and *b* values are arbitrary constants ($\mu gC\ m^{-3}$) that convert the $(OM/OC)_{HOA}$ and $(OM/OC)_{LV\text{-}OOA}$ ratios to the organic mass concentrations of the HOA and the LV-OOA, respectively. The factor "0.3", which is multiplied by the variable *x*, is a factor for the SOA carbon yield based on the laboratory experiments of SOA formation by toluene photooxidation (Irei et al., 2006; Irei et al., 2011). The equation (4) has one variable, *x*, and 6 parameters, four of which are determined by PMF analysis. The greater extent of reaction processing proceeds, the greater LV-OOA contributes to the binary mixture of HOA and LV-OOA, each of which has significantly different f_{44} value. Consequently, the f_{44} of the binary mixture containing a significantly low f_{44} continues to increase until it is saturated with LV-OOA. This hypothesis consistently explains our observations that the f_{44} oxidation indicator sometimes worked, and sometimes did not. There is also a possible limitation that the indicator also depends on distinctive values of f_{44}. As two members, HOA and LV-OOA, had the similar f_{44} values, the indicator would not work.

The f_{44} curve of organic aerosols was calculated using three different combinations of

532 parameters listed in Table 3. It was found that the model calculation underestimated the f_{44}
533 (Figure 8) when 0.05 and 1 μgC m^{-3} were used for the *a* and *b* values, respectively, together
534 with the rest of the parameters obtained from the PMF analysis (*i.e.*, applying the parameters
535 in the combination I in Table 3). Although these *a* and *b* values were used in the previous report
536 and demonstrated reasonable agreement with the observations (*i.e.*, applying the parameters in
537 the combination III), the agreement was owing to different f_{44} values and OM/OC ratios
538 extracted from the PMF analysis (see the Section 3.4). To have reasonable agreement with the
539 observations using the f_{44} and OM/OC extracted by the PMF analysis, the use of 0.0175 and 1
540 μgC m^{-3} for the *a* and *b* values (applying the parameters in the combination II) was found to
541 give the best fitting to the observations.

542 As discussed previously, there was a strong relationship between the NO_x turn over and O_3
543 mixing ratio (Sect. 3.5.1). This relationship can be converted to the one between *t*[OH] and O_3
544 mixing ratios (Figure 9). An obtained linear relationship was $[O_3] = (3.48 \pm 0.06) \times 10^{-7} \times$
545 *t*[OH] + 30.7 ± 0.3. This provides the increasing rate of ozone $(3.48 \pm 0.06) \times 10^{-7} \times$ [OH] ppbv
546 h^{-1} and the background ozone mixing ratio of 30.7 ppbv in this region. If [OH] of 5×10^5
547 molecules cm^{-3} (Takegawa et al., 2007; Irei et al., 2014) is given as the mean concentration of
548 OH radical during the long-range transport in this region, the equation gives the average ozone
549 production rate of 0.174 ppbv h^{-1}. A combination with measurements for OH radical
550 concentration will secure a more accurate production rate of ozone in this region.

4. Summary

To improve our understanding of the ozone and SOA formation from the oxidation of atmospheric pollutants, we conducted field studies from December 2010 to May 2011 on Fukue Island, Nagasaki Prefecture, Japan. Wind-sector analysis of CO mixing ratios revealed that the ratio showed almost no wind-sector dependence, suggesting that the influence of emissions from residential areas near the measurement site was negligible. This fact in turn indicates that the influence of mid- and/or long-range transport of air pollutants to the site had a significant influence. Photochemical age, *t*[OH], was estimated from $[NO_x]/[NO_y]$ and a NMHC concentration ratio, and the validity of the ratios was evaluated. The evaluation suggested that the hydrocarbon clock was significantly influenced by mixing with background air containing 0.16 ppbv of ethyne, a NMHC with a relatively long lifetime, resulting in significant bias in the estimation of *t*[OH]. In contrast, loss of NO_x due to reaction with O_3 at night was not influential to the NO_x/NO_y clock, which thus seemed to function appropriately, at least with respect to relative aging. The *t*[OH] value obtained with the NO_x/NO_y clock was then compared with f_{44} obtained by AMS measurements, and f_{44} was observed to increase with increasing *t*[OH], indicating the f_{44} can also be used as an oxidation indicator. This indicator likely works under the condition where two different types of organic aerosols, such as primary and secondary organic aerosols represented by hydrocarbon-like organic aerosols and low-volatile oxygenated organic aerosol, respectively, are mixed. Using linear regression analysis, we

570 estimated that the f_{44} increase rate for organic aerosols transported over the East China Sea
571 averaged (1.05 ± 0.03) × 10^{-9} × [OH] h^{-1}. This rate was almost identical to the background-
572 corrected rate observed during the New England Air Quality Study in the summer of 2002. The
573 consistency may implying the similar production processe(s) of SOA, possibly humic-like
574 substances. In addition, a clear proportional relationship was observed between O_3 and *t*[OH].
575 According to the linear regression analysis, the increasing rate and background mixing ratio of
576 O_3 in this region were found to be (3.48 ± 0.06) × 10^{-7} × [OH] ppbv h^{-1} and 30.7 ppbv,
577 respectively.

578 **Author Contribution**

579 Satoshi Irei contributed to the AMS, O_3, and meteorological measurements and is the person
580 in charge of the data analysis and writing the manuscript. Akinori Takami is the person in
581 charge of the AMS, O_3, and meteorological measurements. Yasuhiro Sadanaga is the person in
582 charge of the NO_x and NO_y measurements. Seiichiro Yonemura is the person in charge of the
583 CO measurements. Yoko Yokouchi is the person in charge of the NMHC measurements.
584 Susumu Nozoe contributed to the NMHC measurements. Hiroshi Bandow contributed to the
585 NO_x and NO_y measurements.

586 **Acknowledgements** We acknowledge the NOAA Air Resources Laboratory (ARL) for the
587 provision of the HYSPLIT transport and dispersion model and/or READY website
588 (http://www.ready.noaa.gov).This project was financially supported by the Special Research

589 Program from the National Institute for Environmental Studies, Japan (SR-95-2011). The
590 project was partially supported by the International Research Hub Project for Climate Change
591 and Coral Reef/Island Dynamics of University of the Ryukyus and the ESPEC Foundation for
592 Global Environment Research and Technologies (Charitable Trust).

593 **References**

594 Allan, J.D., Delia, A.E., Coe, H., Bower, K.N., Alfarra, M.R., Jimenez, J.L., Middlebrook,
595 A.M., Drewnick, F., Onasch, T.B., Canagaratna, M.R., Jayne, J.T., and Worsnop, D.R.: A
596 generalized method for the extraction of chemically resolved mass spectra from
597 Aerodyne aerosol mass spectrometer data, J. Aerosol Sci., 35, 909–922, 2004.
598 Brown, S.S., Ryerson, T.B., Wollny, A.G., Brock, C.A., Peltier, R., Sullivan, A.P., Weber,
599 R.J., Dube, W.P., Trainer, M., Meagher, J.F., Fehsenfeld, F.C., Ravishankara, A.R.:
600 Variability in nocturnal nitrogen oxide processing and its role in regional air quality,
601 Science, 311, 67, 67-70, doi: 10.1126/science.1120120, 2006.
602 de Gouw, J.A., Middlebrook, A.M., Warneke, C., Goldan, P.D., Kuster, W.C., Roberts, J.M.,
603 Fehsenfeld, F.C., Worsnop, D.R., Canagaratna, M.R., Pszenny, A.A.P., Keene, W.C.,
604 Marchewka, M., Bertman, S.B., and Bates, T.S.: Budget of organic carbon in a polluted
605 atmosphere: Results from the New England Air Quality Study in 2002, J. Geophys. Res.:
606 Atmos., 110, doi:10.1029/2004JD005623, 2005.
607 Draxler, R.R. and Rolph, G.D.: HYSPLIT (Hybrid Single-Particle Lagrangian Integrated

608 Trajectory) Model Access via NOAA ARL READY. NOAA Air Resources Laboratory,
609 College Park, MD. http://www.arl.noaa.gov/HYSPLIT.php., 2013.
610 Ebben, C.J., Strick, B.F., Upshur, M.A., Chase, H.M., Achtyl, J.L., Thomson, R.J., Geiger,
611 F.M.: Towards the identification of molecular constituents associated with the surfaces of
612 isoprene-derived secondary organic aerosol (SOA) particles. Atmos. Chem. Phys., 14,
613 2303–2314, 2014.
614 Finlayson-Pitts, B.J. and Pitts, Jr. J.N.: Chemistry of the upper and lower atmosphere,
615 Academic Press, San Diego, California, U.S.A., 2000.
616 Grosjean, D. and Seinfeld, J.H.: Parameterization of the formation potential of secondary
617 organic aerosols. *Atmos. Environ.*, *23*, 1733–1747, 1989.
618 Irei, S., Huang, L., Collin, F., Zhang, W., Hastie, D., Rudolph, J.: Flow reactor studies of the
619 stable carbon isotope composition of secondary particulate organic matter generated by
620 OH-radical induced reaction of toluene. *Atmos. Environ.*, *40*, 5858–5867, 2006
621 Irei, S., Rudolph, J., Huang, L., Auld, J., Hastie, D.: Stable carbon isotope ratio of secondary
622 particulate organic matter formed by photooxidation of toluene in indoor smog chamber.
623 *Atmos. Environ.*, *45*, 856–862, 2011.
624 Irei, S., Takami, A., Hayashi, M., Sadanaga, Y., Hara, K., Kaneyasu, N., Sato, K., Arakaki, T.,
625 Hatakeyama, S., Bandow, H., Hikida, T., and Shimono, A.: Transboundary secondary
626 organic aerosol in western Japan indicated by the $\delta^{13}C$ of water-soluble organic carbon

627 and the *m*/*z* 44 signal in organic aerosol mass spectra, Environ. Sci. Technol., 48, 11,
628 6273–6281, 2014.
629 Irei, S., Takami, A., Sadanaga, Y., Miyoshi, T., Arakaki, T., Sato, K., Kaneyasu, N., Bandow,
630 H., and Hatakeyama, S.: Transboundary secondary organic aerosol in western Japan: An
631 observed limitation of the f_{44} oxidation indicator, Atmos. Environ., 120, 71–75, 2015.
632 Jayne, J.T., Leard, D.C., Zhang, X., Davidovits, P., Smith, K.A., Kolb, C.E., and Worsnop,
633 D.R.: Development of an aerosol mass spectrometer for size and composition analysis of
634 submicron particles, Aerosol Sci. Technol., 33, 49–70, 2000.
635 Jimenez, J.L., Canagaratna, M.R., Donahue, N.M., Prevot, A.S.H., Zhang, Q., Kroll, J.H.,
636 DeCarlo, P.F., Allan, J.D., Coe, H., Ng, N.L., Aiken, A.C., Docherty, K.D., Ulbrich, I.M.,
637 Grieshop, A.P., Robinson, A.L., Duplissy, J., Smith, J. D., Wilson, K.R., Lanz, V.A.,
638 Hueglin, C., Sun, Y.L., Laaksonen, A., Raatikainen, T., Rautiainen, J., Vaattovaara, P.,
639 Ehn, M., Kulmala1, M., Tomlinson, J.M., Collins, D.R., Cubison, M.J., Dunlea, E.J.,
640 Huffman, J.A., Onasch, T.B., Alfarra, M.R., Williams, P.I., Bower, K., Kondo, Y.,
641 Schneider, J., Drewnick, F., Borrmann, S., Weimer, S., Demerjian, K., Salcedo, D.,
642 Cottrell, L., Griffin, R., Takami, A., Miyoshi, T., Hatakeyama, S., Shimono, A., Sun, J.Y.,
643 Zhang, Y.M., Dzepina, K., Kimmel, J.R., Sueper, D., Jayne, J.T., Herndon, S.C.,
644 Trimborn, A.M., Williams, L.R., Wood, E.C., Kolb, C.E., Baltensperger, U., and
645 Worsnop, D.R.: Evolution of organic aerosols in the atmosphere, Science, 326, 1525–

646 1529, 2009.
647 Kanaya, Y., Tanimoto, H., Yokouchi, Y., Taketani, F., Komazaki, Y., Irie, H., Takashima, H.,
648 Pan, X., Nozoe, S., and Inomata, S.: Diagnosis of photochemical ozone production rates
649 and limiting factors in continental outflow air masses reaching Fukue Island, Japan:
650 Ozone-control implications. Aerosol Air Qual. Res., 16, 430-441, 2016.
651 Kato, S., Kajii, Y., Itokazu, R., Hirokawa, J., Koda, S., Kinjo, Y.: Transport of atmospheric
652 carbon monoxide, ozone, and hydrocarbons from Chinese coast to Okinawa Island in the
653 western Pacific during winter. Atmos. Environ., 38, 2975–2981, 2004.
654 Kim, C.-H., Park, S.-Y., Kim, Y.-J., Chang, L.-S., Song, S.-K., Moon, Y.-S., and Song, C.-K.:
655 A numerical study on indicators of long-range transport potential for anthropogenic
656 particulate matters over northeast Asia, Atmos. Environ., 58, 35–44, 2012.
657 Kleinman, L.I., Daum, P.H., Lee, Y.-N., Senum, G.I., Springston, S.R., Wang, J., Berkowitz,
658 C., Hubbe, J., Zaveri, R.A., Brechtel, F.J., Jayne, J., Onasch, T.B., and Worsnop, D.:
659 Aircraft observations of aerosol composition and ageing in New England and Mid-
660 Atlantic States during the summer 2002 New England Air Quality Study field campaign,
661 J. Geophys. Res.: Atmos., 112, doi:10.1029/2006JD007786, 2007.
662 Kurokawa, J., Ohara, T., Morikawa, T., Hanayama, S., Janssens-Maenhout, G., Fukui, T.,
663 Kawashima, K., Akimoto, H.: Emissions of air pollutants and greenhouse gases over
664 Asian regions during 2000–2008: Regional Emission inventory in ASia (REAS) version

665 2, Atmos. Chem. Phys., 13, 11019-11058, 2013.
666 Liggio, J., Li, S-M, Vlasenko, A., Sjostedt, S., Chang, R., Shantz, N., Abbatt, J., Slowik, J.G.,
667 Bottenheim, J.W., Brickell, P.C., Strond, C., and Leaitch, R.W.: Primary and secondary
668 organic aerosols in urban air masses intercepted at a rural site, J. Geophys. Res.: Atmos.,
669 115, doi:10.1029/2010JD014426, 2010.
670 McKeen, S.A. and Liu, S.C.: Hydrocarbon ratios and photochemical history of air masses,
671 Geophys. Res. Lett., 20, 2363–2366, 1993.
672 Ng, N. L., Canagaratna, M.R., Zhang, Q., Jimenez, J.L., Tian, J., Ulbrich, I.M., Kroll, J.H.,
673 Docherty, K.S., Chhabra, P.S., Bahreini, R., Murphy, S.M., Seinfeld, J.H., Hildebrandt,
674 L., Donahue, N.M., DeCarlo, P.F., Lanz, V.A., Prevot, A.S.H., Dinar, E., Rudich, Y. and
675 Worsnop, D.R.: Organic aerosol components observed in Northern Hemispheric datasets
676 from Aerosol Mass Spectrometry, Atmos. Chem. Phys., 10, 4625–4641, 2010.
677 Olszyna, K.J., Bailey, E.M., Simonaitis, R., and Meagher, J.F.: O_3 and NO_y relationships at a
678 rural site, J. Geophys. Res.: Atmos., 99(D7), 14,557–14,563, 1994.
679 Pandey Deoral, S., Brunner, D., Steinbacher, M., Weers, U., Staehelin, J.: Long-term in situ
680 measurements of NOx and NOy at Jungfraujoch 1998–2009: time series analysis and
681 evaluation, Atmos. Chem. Phys., 12, 2551–2566, 2012.
682 Parrish, D.D., Hahn, C.J., Williams, E.J., Norton, R.B., Fehsenfeld, F.C.: Indications of
683 photochemical histories of pacific air masses from measurements of atmospheric trace

684 species at Point Arena, California, J. Geophys. Res.: Atmos., 97, D14, 15883–15901,
685 1992.
686 Pochanart, P., Akimoto, H., Kinjo, Y., and Tanimoto, H.: Surface ozone at four remote island
687 sites and the preliminary assessment of the exceedances of its critical level in Japan,
688 *Atmos. Environ.*, 36, 4235–4250, 2002.
689 Roberts, J.M., Fehsenfeld, F.C., Liu, S.C., Bollinger, M.J., Hahn, Carole, Albritton, D.L.,
690 Sievers, R.E.: Measurements of aromatic hydrocarbon ratios and NOx concentrations in
691 the rural troposphere: Observations of air mass photochemical aging and NOx removal,
692 Atmos. Environ., 18, 2414–2432, 1984.
693 Roussel, P.B., Lin, X., Camacho, F., Laszlo, S., Taylor, R., Melo, O., Shepson, P.B., Hastie,
694 D., and Melo, O.T.: Observations of ozone and precursor levels at two sites around
695 Toronto, Ontario, during SONTOS 92, Atmos. Environ., 30(12), 2145–2155, 1996.
696 Rudolph, J. and Johnen, F.J.: Measurements of light atmospheric hydrocarbons over the
697 Atlantic in regions of low biological activity, J. Geophys. Res.: Atmos., 95, D12, 20583–
698 20591, 1990.
699 Sadanaga, Y., Fukumori, Y., Kobashi, T., Nagata, M., Takenaka, N., and Bandow, H.:
700 Development of a selective light-emitting diode photolytic NO_2 converter for
701 continuously measuring NO_2 in the atmosphere, Anal. Chem., 82, 9234–9239, 2010.
702 Seinfeld, J.H. and Pandis, S.N.: Atmospheric Chemistry and Physics, A Wiley Interscience

703 Publication, New York, U.S.A., 1997.

704 Suthawaree, J., Kato, S., Takami, A., Kadena, H., Toguchi, M., Yogi, K., Hatakeyama, S., and
705 Kajii, Y.: Observation of ozone and carbon monoxide at Cape Hedo, Japan: Seasonal
706 variation and influence of long-range transport, *Atmos. Environ.* 42, 2971–2981, 2008.

707 Takami, A., Miyoshi, T., Shimono, A., and Hatakeyama, S.: Chemical composition of fine
708 aerosol measured by AMS at Fukue Island, Japan during APEX period, Atmos. Environ.,
709 39, 4,913–4,924, 2005.

710 Takami, A., Miyoshi, T., Shimono, A., Kaneyasu, N., Kato, S., Kajii, Y., and Hatakeyama,
711 S.: Transport of anthropogenic aerosols from Asia and subsequent chemical
712 transformation, J. Geophys. Res.: Atmos., *112*, D22S31, doi:10.1029/2006JD008120,
713 2007.

714 Takegawa, N., Kondo, Y., Koike, M., Chen, G., Machida, T., Watai, T., Blake, D.R., Streets,
715 D.G., Woo, J.-H., Carmichael, G.R., Kita, K., Miyazaki, Y., Shirai, T., Liley, J.B., and
716 Ogawa, T.: Removal of NOx and NOy in Asian outflow plumes: Aircraft measurements
717 over the western Pacific in January 2002. J. Geophys. Res.: Atmos., 109, D23S04, 2004.

718 Takegawa, N., Miyakawa, T., Kondo, Y., Blake, D.R., Kanaya, Y., Koike, M., Fukuda, M.,
719 Komazaki, Y., Miyazaki, Y., Shimono, A., and Takeuchi, T.: Evolution of submicron
720 organic aerosol in polluted air exported from Tokyo, Geophys. Res. Lett., 33,
721 doi:10.1029/2006GL025815, 2006.

722 Takiguchi, Y., Takami, A., Sadanaga, Y., Lun, X., Shimizu, A., Matsui, I., Sugimoto, N.,

723 Wang, W., Bandow, H., and Hatakeyama, S.: Transport and transformation of total
724 reactive nitrogen over the East China Sea, J. Geophys. Res.: Atmos., 113,
725 doi:10.1029/2007JD009462, 2008.
726 Tang, J.H., Chan, L.Y., Chang, C.C., Liu, S., and Li, Y.S.: Characteristics and sources of non-
727 methane hydrocarbons in background atmospheres of eastern, southwestern, and
728 southern China, J. Geophys. Res.: Atmos., 114, doi:10.1029/2008JD010333, 2009.
729 Tanimoto, H., Sawa, Y., Yonemura, S., Yumimoto, K., Matsueda, H., Uno, I., Hayasaka, T.,
730 Mukai, H., Tohjima, Y., Tsuboi, K., and Zhang, L.: Diagnosing recent CO emissions and
731 ozone evolution in East Asia using coordinated surface observations, adjoint inverse
732 modeling, and MOPITT satellite data, Atmos. Chem. Phys., 8, 3867–3880, 2008.
733 Ulbrich, I.M., Canagaratna, M.R., Zhang, Q., Worsnop, D.R., and Jimenez, J.L.:
734 Interpretation of organic components from Positive Matrix Factorization of aerosol mass
735 spectrometric data, Atmos. Chem. Phys., 9, 2891–2918, 2009.
736 Yokouchi Y.: Development of real-time monitoring system for non-methane hydrocarbons in
737 the atmosphere, Final Report for Environmental Technology Development Fund,
738 Ministry of the Environment (in Japanese), 2008.
739 Yokouchi Y., Takami, A., and Ohara, T.: Observational and modeling study of the high-ozone
740 episode in northern Kyusyu focused on the impact of ozone precursors, Report of Special
741 Research from the National Institute for Environmental Studies, Japan (in Japanese),

2011.

Yuba, A., Sadanaga, Y., Takami, A., Hatakeyama, S., Takenaka, N., and Bandow, H.: Measurement system for particulate nitrate based on the scrubber difference NO-O_3 chemiluminescence method in remote areas, Anal. Chem., 82, 8916–8921, 2010.

Wang, M., Shao, M., Chen, W., Lu, S., Liu, Y., Yuan, B., Zhang, Q., Zhang, Q., Chang, C.-C., Wang, B., Zeng, L., Hu, M., Yang, Y., and Li, Y.: Trends of non-methane hydrocarbons (NMHC) emissions in Beijing during 2002-2013. Atmos. Chem. Phys., 15, 1489–1502, 2015.

Zhang, Q. Worsnop, D.R., Canagaratna, M.R., and Jimenez, J.L.: Hydrocarbon-like and oxygenated organic aerosols in Pittsburgh: insights into sources and processes of organic aerosols. Atmos. Chem. Phys., 5, 3289–3311, 2005.

761

762

763 Figure captions

764

765 Figure 1. Location of the Fukue Island monitoring station.

766

767 Figure 2. Extracted mass spectra from two-factorial PMF analysis: top, mass spectra identified
768 as hydrocarbon-like organic aerosol (HOA); bottom, mass spectra identified as low-volatile
769 oxygenated organic aerosol (LV-OOA).

770

771 Figure 3. Temporal variation of mass concentration of HOA (orange) and LV-OOA (green)
772 obtained by PMF analysis.

773

774 Figure 4. Plot of f_{44} versus f_{43} for different types of organic aerosols extracted from PMF
775 analysis. Dashed lines are the limits of oxidation states reported by Ng et al. (2010).

776

777 Figure 5. Scatter plot of natural logarithm of $[NO_x]/[NO_y]$ ratio versus O_3 mixing ratio. The
778 data points with the ozone mixing ratios less than 25 ppbv were excluded from the linear
779 regression.

780

781 Figure 6. Time-series variation of photochemical age, *t*[OH], estimated from $[NO_x]/[NO_y]$
782 ratios.

783

784 Figure 7. Scatter plot of natural logarithm of [toluene]/[ethyne] ratio as function of natural
785 logarithm of [*i*-pentane]/[ethyne] ratio (gray dots). Linear regressions shown are calculated
786 depletion trends resulting from mixing with background air (dotted lines) and from reaction
787 with OH radicals (solid lines); these trends were determined by using the initial NMHC ratios
788 from the literature, for vehicular emissions 1 (black open circle), vehicular emissions 2 (red

open circle), solvent use (green open circle), and natural gas and gasoline leakage (blue open circle) observed in Beijing (Wang et al., 2015), as well as field measurement data obtained at Lin'an, a rural background site in the Yangtze River Delta, China (yellow open circle) from Tang et al. (2009). The brown open circle that all the dotted lines meet at corresponds to the background values observed at Cape Hedo (Kato et al., 2004). See the text for the calculation and references for these data.

Figure 8. Scatter plot of hourly averaged f_{44} (black dot) as function of photochemical age, t[OH], estimated by means of the NO_x/NO_y clock (the bottom x-axis) and a linear regression (grey line). As comparison, f_{44} binary mixing models (dotted curves) of HOA and LV-OOA using different combinations of model parameters (combination I (green); combination II (blue); and combination III (red)) are also shown. See the text for the detail of the combinations of model parameters.

Figure 9. Scatter plot of ozone mixing ratio versus photochemical age (t[OH]). The data points with the ozone mixing ratios less than 25 ppbv were excluded from the linear regression.

816

817

818 **Table 1. Concentrations and mixing ratios of chemical species observed during the study**
819 **period.**

	Number of data	Mean	SD	Min[a]	Max	Lower quartile	Median	Upper quartile
Fine PM		(μg m^{-3})						
Chloride		0.08	0.12	LDL	2.65	0.03	0.04	0.09
Ammonium		1.5	1.6	LDL	14.7	0.6	1.1	1.8
Nitrate		0.69	1.43	LDL	22.00	0.12	0.25	0.63
Sulfate		4.2	3.3	LDL	23.8	2.0	3.4	5.5
Organics	22726	2.7	1.9	LDL	24.5	1.4	2.2	3.4
Total[b]		9.2	7.4	0.02	66.7	4.7	7.5	11.2
m/*z* 43 in organics		0.18	0.14	LDL	4.17	0.08	0.14	0.22
m/*z* 44 in organics		0.40	0.30	0.06	2.45	0.20	0.33	0.50
m/*z* 57 in organics		0.03	0.04	0.01	1.87	0.02	0.03	0.04
Gas-phase species		(ppbv)						
CO	4163	230	102	57	1136	160	204	272
NO	4176	0.06	0.16	LDL	4.45	LDL	LDL	0.06
NO_x	4176	1.39	1.16	LDL	12.70	0.70	1.10	1.70
NO_y	4163	4.86	3.49	0.13	25.41	2.49	3.95	6.03
O_3	4165	45	11	10	97	38	45	52
i-Pentane	3856	0.106	0.079	LDL	2.055	0.066	0.098	0.132
Toluene	3856	0.110	0.142	LDL	2.625	0.044	0.071	0.123
Ethyne	3856	0.496	0.326	0.014	4.442	0.304	0.407	0.597

820 [a]LDL: lower than detection limit.

821 [b]Sum of chloride, ammonium, nitrate, sulfate, and organics.

822

Table 2. Coefficients of determination for correlations between chemical species concentrations.

	PM_NH_4	PM_NO_3	PM_SO_4	PM_org	*m/z* 43	*m/z* 44	*m/z* 57	O_3	NO_x	NO_y	CO	*i*-Pentane	Toluene	Ethyne
PM_NH_4	1	0.693	0.639	0.696	0.443	0.755	0.323	0.251	0.007	0.480	0.405	0.004	0.026	0.097
PM_NO_3	0.693	1	0.263	0.529	0.389	0.521	0.320	0.145	0.035	0.544	0.314	0.025	0.051	0.107
PM_SO_4	0.639	0.263	1	0.430	0.380	0.463	0.191	0.128	0.001	0.179	0.371	0.013	0.006	0.125
PM_org	0.696	0.529	0.430	1	0.747	0.949	0.606	0.303	0.053	0.559	0.562	0.060	0.081	0.198
m/z 43	0.443	0.389	0.380	0.747	1	0.640	0.588	0.146	0.153	0.459	0.543	0.100	0.094	0.301
m/z 44	0.755	0.521	0.463	0.949	0.640	1	0.471	0.384	0.016	0.510	0.526	0.007	0.039	0.142
m/z 57	0.323	0.320	0.191	0.606	0.588	0.471	1	0.098	0.160	0.417	0.394	0.106	0.137	0.236
O_3	0.251	0.145	0.128	0.303	0.146	0.384	0.098	1	0.007	0.292	0.288	0.013	0.006	0.053
NO_x	0.007	0.035	0.001	0.053	0.153	0.016	0.160	0.007	1	0.309	0.136	0.195	0.225	0.221
NO_y	0.480	0.544	0.179	0.559	0.459	0.510	0.417	0.292	0.309	1	0.674	0.117	0.155	0.422
CO	0.405	0.314	0.371	0.562	0.543	0.526	0.394	0.288	0.136	0.674	1	0.193	0.126	0.724
i-Pentane	0.004	0.025	0.013	0.060	0.100	0.007	0.106	0.013	0.195	0.117	0.193	1	0.410	0.435
Toluene	0.026	0.051	0.006	0.081	0.094	0.039	0.137	0.006	0.225	0.155	0.126	0.410	1	0.302
Ethyne	0.097	0.107	0.125	0.198	0.301	0.142	0.236	0.053	0.221	0.422	0.724	0.435	0.302	1

Table 3. Three different combinations of model parameters.

Parameters	Combination I[a]	Combination II[a]	Combination III[b]
a ($\mu gC\ m^{-3}$)	0.05	0.0175	0.05
b ($\mu gC\ m^{-3}$)	1	1	1
$^{HOA}f_{44}$	0	0	0.08
$^{LV\text{-}OOA}f_{44}$	0.237	0.2371	0.22
$(OM/OC)_{HOA}$ ($\mu g\ \mu gC^{-1}$)	2.9	2.9	1.2
$(OM/OC)_{LV\text{-}OOA}$ ($\mu g\ \mu gC^{-1}$)	5.0	5.0	3.7

[a]The f_{44} and OM/OC values for HOA and LV-OOA are based on the results from the PMF analysis.

[b]Parameters used in the previous report (Irei et al., 2014, supportive information).

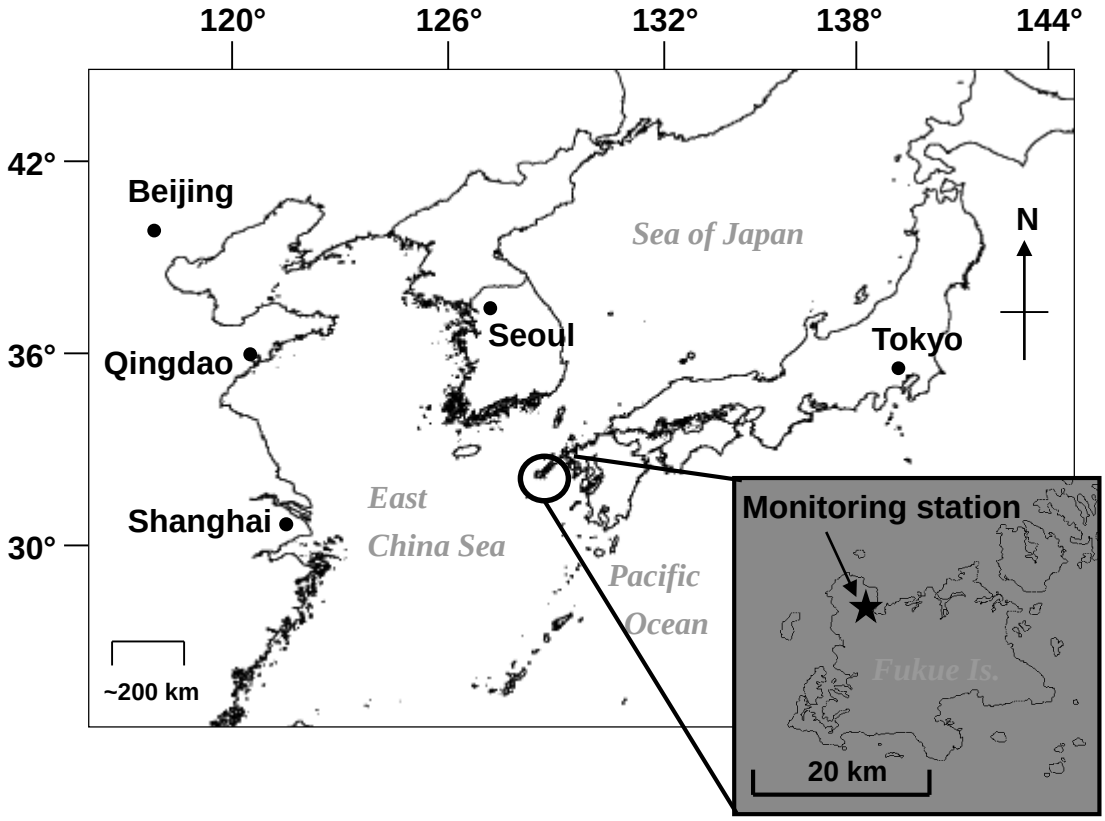

Figure 1. Location of the Fukue Island monitoring station.

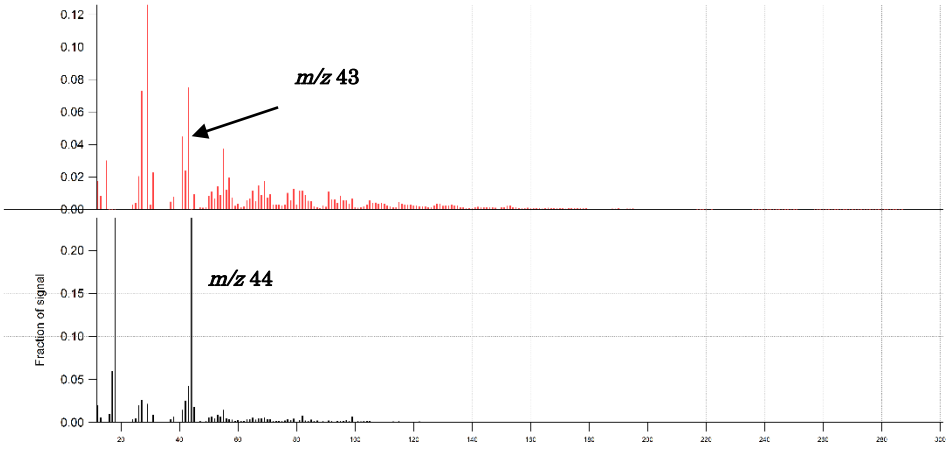

Figure 2. Extracted mass spectra from two-factorial PMF analysis: top, mass spectra identified as hydrocarbon-like organic aerosol (HOA); bottom, mass spectra identified as low-volatile oxygenated organic aerosol (LV-OOA).

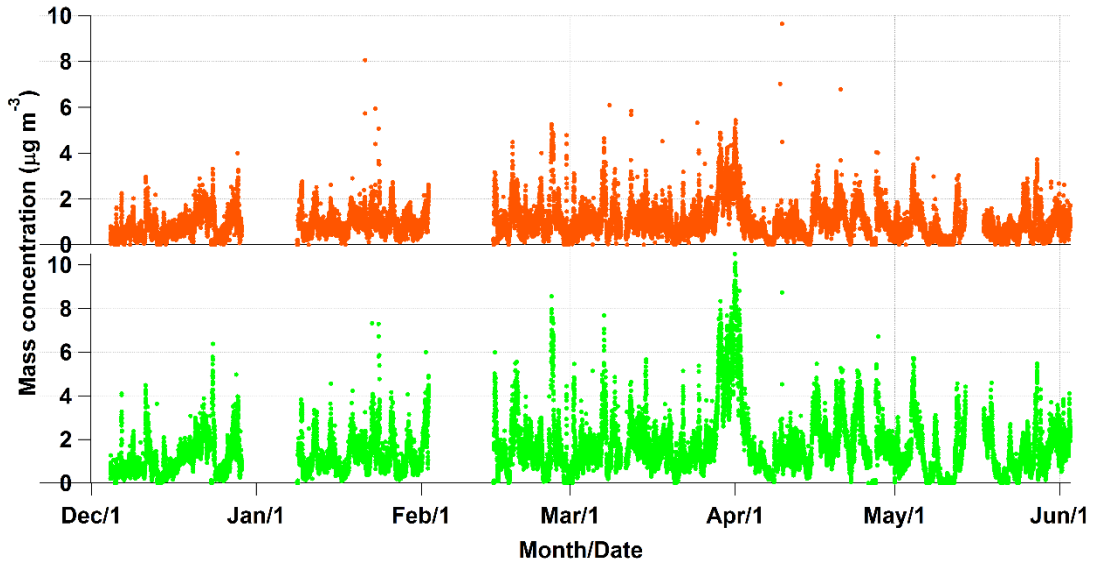

Figure 3. Temporal variation of mass concentration of HOA (orange) and LV-OOA (green) obtained by PMF analysis.

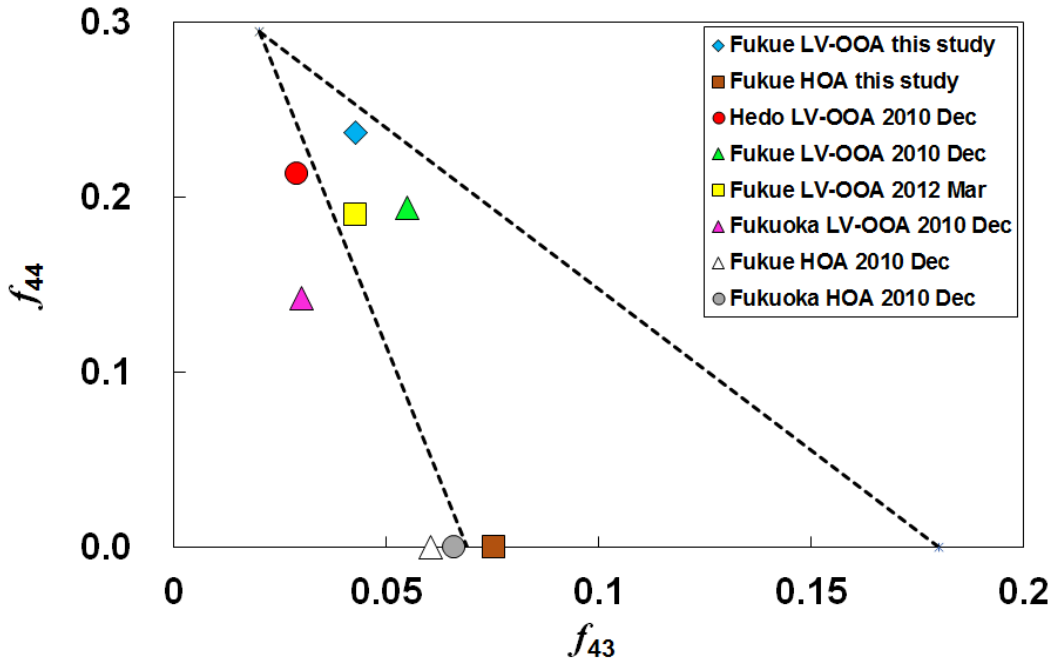

Figure 4. Plot of f_{44} versus f_{43} for different types of organic aerosols extracted from PMF analysis. Dashed lines are the limits of oxidation states reported by Ng et al. (2010).

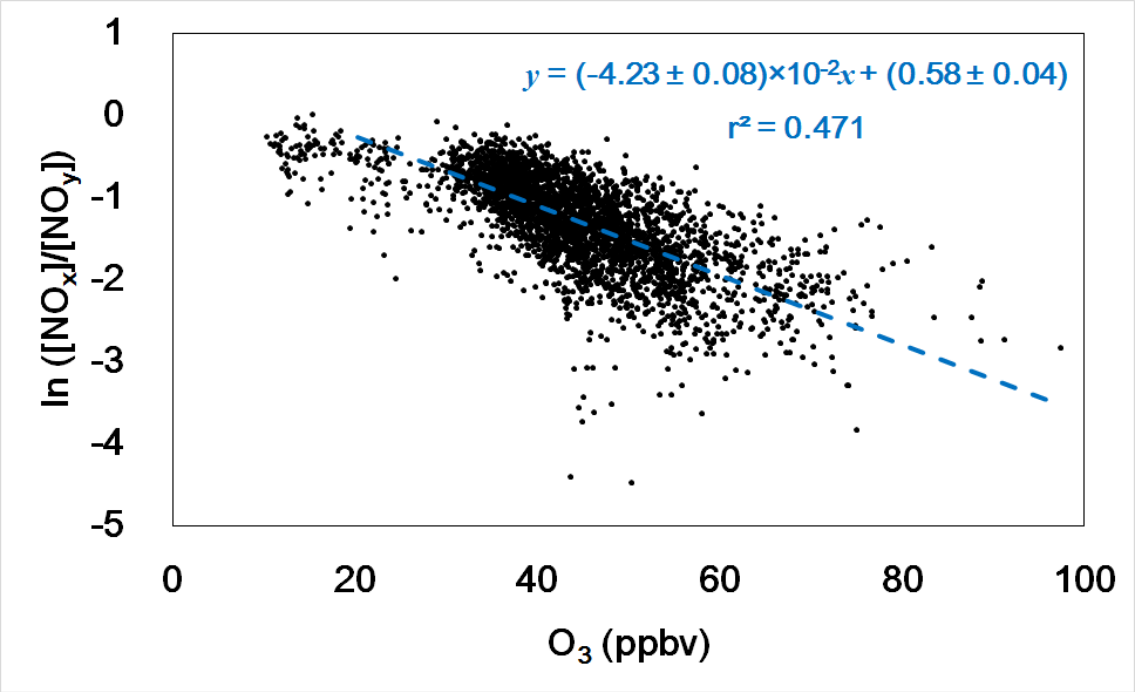

Figure 5. Scatter plot of natural logarithm of $[NO_x]/[NO_y]$ ratio versus O_3 mixing ratio. The data points with the ozone mixing ratios less than 25 ppbv were excluded from the linear regression.

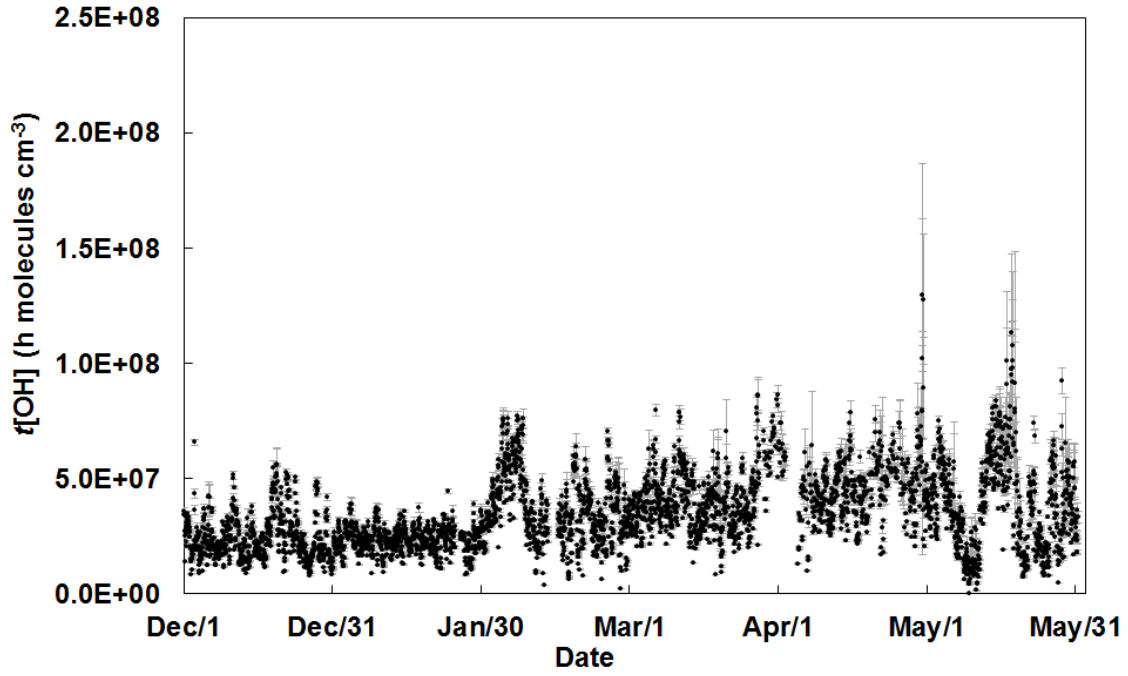

Figure 6. Time-series variation of photochemical age, *t*[OH], estimated from $[NO_x]/[NO_y]$ ratios.

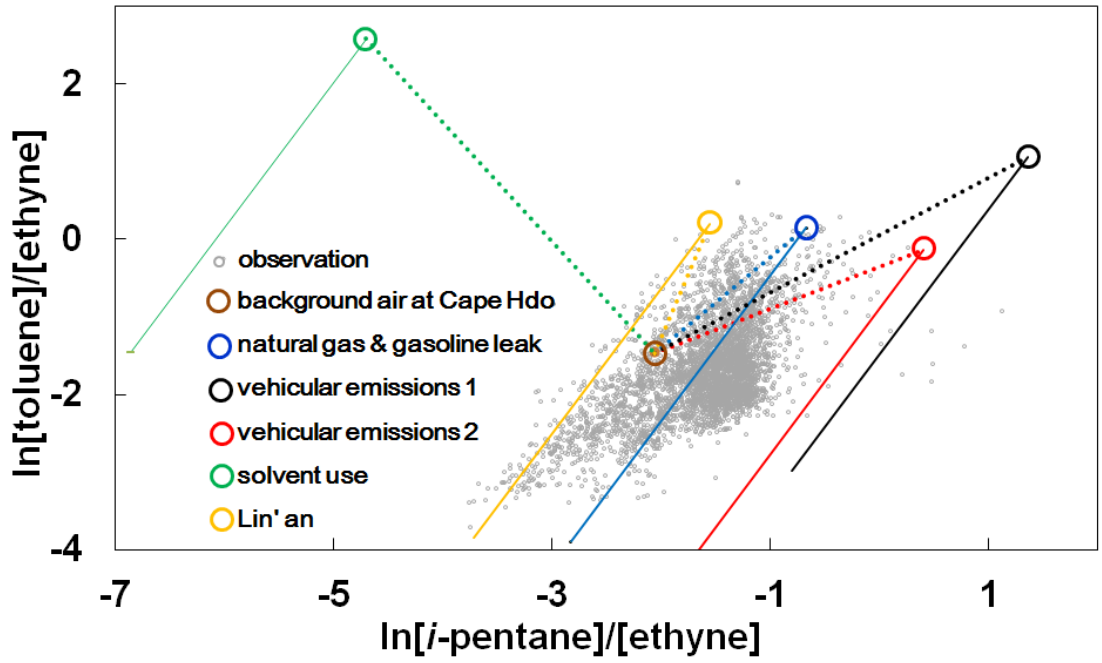

Figure 7. Scatter plot of natural logarithm of [toluene]/[ethyne] ratio as function of natural logarithm of [*i*-pentane]/[ethyne] ratio (gray dots). Linear regressions shown are calculated depletion trends resulting from mixing with background air (dotted lines) and from reaction with OH radicals (solid lines); these trends were determined by using the initial NMHC ratios from the literature, for vehicular emissions 1 (black open circle), vehicular emissions 2 (red open circle), solvent use (green open circle), and natural gas and gasoline leakage (blue open circle) observed in Beijing (Wang et al., 2015), as well as field measurement data obtained at Lin'an, a rural background site in the Yangtze River Delta, China (yellow open circle) from Tang et al. (2009). The brown open circle that all the dotted lines meet at corresponds to the background values observed at Cape Hedo (Kato et al., 2004). See the text for the calculation and references for these data.

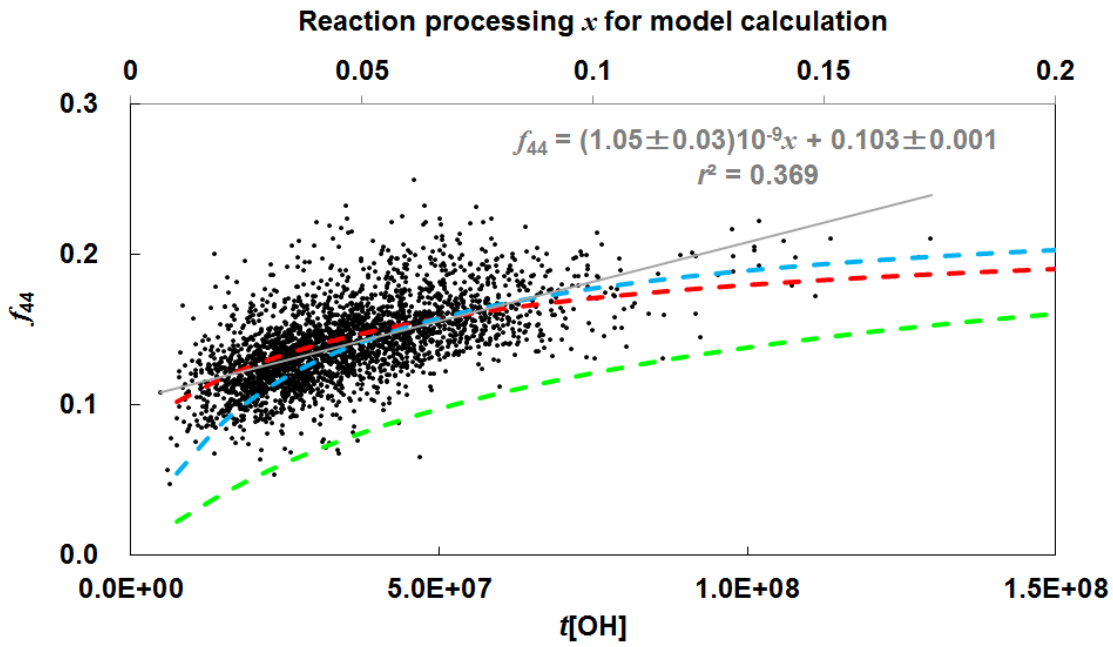

Figure 8. Scatter plot of hourly averaged f_{44} (black dot) as function of photochemical age, t[OH], estimated by means of the NO_x/NO_y clock (the bottom x-axis) and a linear regression (grey line). As comparison, f_{44} binary mixing models (dotted curves) of HOA and LV-OOA using different combinations of model parameters (combination I (green); combination II (blue); and combination III (red)) are also shown. See the text for the detail of the combinations of model parameters.

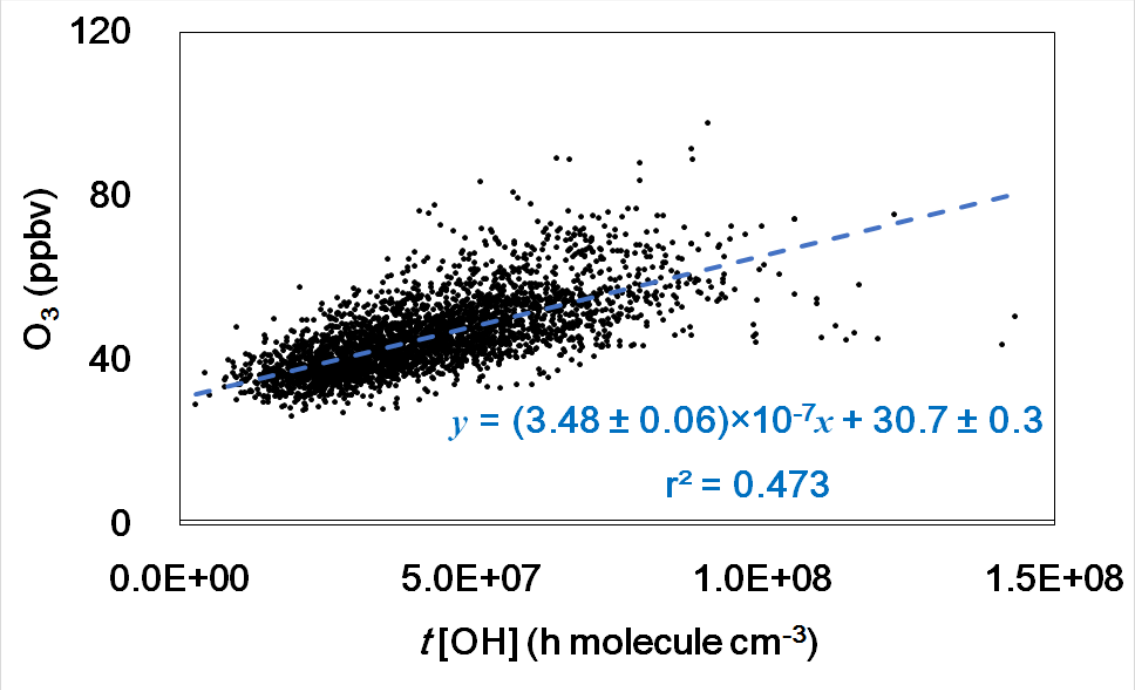

Figure 9. Scatter plot of ozone mixing ratio versus photochemical age (t[OH]). The data points with the ozone mixing ratios less than 25 ppbv were excluded from the linear regression.